IMMUNOLOGY

Detection of response to tumor microenvironment–targeted cellular immunotherapy using nano-radiomics

Laxman Devkota[1,2]*, Zbigniew Starosolski[1,3]*, Charlotte H. Rivas[2,4], Igor Stupin[1], Ananth Annapragada[1,3], Ketan B. Ghaghada[1,3]†, Robin Parihar[2,4]†

Immunotherapies, including cell-based therapies, targeting the tumor microenvironment (TME) result in variable and delayed responses. Thus, it has been difficult to gauge the efficacy of TME-directed therapies early after administration. We investigated a nano-radiomics approach (quantitative analysis of nanoparticle contrast–enhanced three-dimensional images) for detection of tumor response to cellular immunotherapy directed against myeloid-derived suppressor cells (MDSCs), a key component of TME. Animals bearing human MDSC-containing solid tumor xenografts received treatment with MDSC-targeting human natural killer (NK) cells and underwent nanoparticle contrast–enhanced computed tomography (CT) imaging. Whereas conventional CT-derived tumor metrics were unable to differentiate NK cell immunotherapy tumors from untreated tumors, nano-radiomics revealed texture-based features capable of differentiating treatment groups. Our study shows that TME-directed cellular immunotherapy causes subtle changes not effectively gauged by conventional imaging metrics but revealed by nano-radiomics. Our work provides a method for noninvasive assessment of TME-directed immunotherapy potentially applicable to numerous solid tumors.

INTRODUCTION

Cellular immunotherapies such as chimeric antigen receptor (CAR)–bearing T cells have shown efficacy in clinical trials of hematologic malignancies (*1*). However, the efficacy in patients with advanced solid tumors has been low (*2*). Solid tumors have inhibitory microenvironments that limit the efficacy of targeted therapies (*3*). Myeloid-derived suppressor cells (MDSCs) play a central role in maintaining the tumor microenvironment (TME) of these solid tumors by suppressing host immunity, establishing new vasculature, and remodeling tissue with tumor-supportive stromal elements (*4*). The frequency of intratumoral MDSCs correlates with cancer stage, disease progression, and resistance to standard chemo- and radiotherapy (*5*). Hence, effective immunotherapy for solid tumors will involve strategies that reverse the inhibitory environment by targeting key components of the TME such as MDSCs. As TME-directed therapies emerge, methods to detect changes within the TME will be required to monitor their efficacy.

Response to TME-directed immunotherapy has been difficult to assess by biopsy due to tumor heterogeneity and the impracticality of repeated biopsy. In vivo imaging provides a noninvasive approach for studying "whole-tumor" dynamics in four-dimensional (4D) domain (3D space + time) and therefore allows the elucidation of inter- and intratumor heterogeneity that is not appreciated using analysis of biopsy samples or 2D microscopy-based techniques (*6*, *7*). However, standard imaging-derived tumor metrics, such as tumor volume derived from conventional computed tomography (CT) and magnetic resonance imaging (MRI), are likely to be ineffective in the assessment of early efficacy of TME-directed therapies. This is because (i) the burden of immunosuppressive cells is substantially low compared with tumor cells in solid tumors, and thus, acute changes in tumor size may not be evident despite alterations in immunosuppressive components like MDSCs, and (ii) the effects of TME-directed therapies on tumor growth are often indirect and delayed (*8*, *9*). Thus, there is a need to investigate advanced imaging methods that may provide early biomarkers of efficacy to immune-based TME-directed therapies.

Radiomics is an emerging field in which 3D images are analyzed to extract quantitative imaging features such as intensity, shape, size, morphology, and texture that can objectively define phenotypic characteristics of tumors (*10*, *11*). These quantitative methods may enable detection of subtle changes in tumor morphology that are not evident by standard imaging tumor metrics. While such methods have been investigated to evaluate tumor response to checkpoint blockade therapies, no preclinical or clinical studies have been conducted to investigate their utility in the context of cellular immunotherapies. Because of increasing interest and ongoing clinical trials in the emerging field of cell-based cancer therapies, we investigated whether the application of radiomics to the human TME would allow for detection of subtle changes in tumor morphology produced after TME-directed cellular immunotherapy.

In prior work, we reported a preclinical xenograft TME model in which human solid tumor cells grow in the presence of human MDSCs and reported the efficacy of gene-modified human natural killer (NK) cells in depleting intratumoral MDSCs (*12*). NK cells modified to express a chimeric version of the NK cytotoxicity receptor NKG2D, whose ligands are overexpressed on human MDSCs, directly lysed human MDSCs and secreted immune-promoting cytokines. Furthermore, we showed that depletion of MDSCs via gene-modified NK cells by itself did not result in tumor regression or improvement in overall survival but did create a more favorable TME that allowed enhanced antitumor activity of subsequently infused tumor-redirected T cells (*12*). Thus, we established a model to study the immediate effects of TME-directed cellular immunotherapy that affects immunosuppressive components of the TME such as MDSCs but without mediating direct antitumor effects.

[1]Singleton Department of Pediatric Radiology, Texas Children's Hospital, Houston, TX, USA. [2]Department of Pediatrics, Section of Hematology-Oncology, Baylor College of Medicine, Houston, TX, USA. [3]Department of Radiology, Baylor College of Medicine, Houston, TX, USA. [4]Center for Cell and Gene Therapy, Texas Children's Hospital, Houston Methodist Hospital, and Baylor College of Medicine, Houston, TX, USA.
*These authors contributed equally to this work.
†Corresponding author. Email: kbghagha@texaschildrens.org (K.B.G.); rparihar@bcm.edu (R.P.)

In the current work, we have further characterized the immunosuppressive nature of this unique preclinical TME model and used it to investigate radiomic phenotypes indicative of response to MDSC-directed cellular immunotherapy. Because MDSCs play a central role in angiogenesis and shaping of tumor vasculature, radiomic analysis was performed on high-resolution contrast-enhanced CT images acquired using a long circulating nanoparticle contrast agent. The long blood half-life and the unique ability of nanoparticles to extravasate and accumulate in perivascular regions of high vascular permeability facilitate 3D interrogation of MDSC-influenced tumor vascular architecture (*13*, *14*). Thus, radiomic analysis of nanoparticle contrast–enhanced CT imaging features was used to follow changes in MDSC composition within the TME. We use the term "nano-radiomics" to refer to radiomic analysis of nanoparticle contrast–enhanced images and report the first of its kind study. We show that nano-radiomic analysis allows the extraction of quantitative features associated with response to MDSC-directed cellular immunotherapy, a clinically useful finding that may be readily applied during cellular therapy trials to noninvasively assess changes in the TME.

RESULTS

Response to MDSC-directed cellular immunotherapy does not correlate with change in overall tumor size

To evaluate the effects of cellular immunotherapy that targets a component of the TME, we used NK cells genetically modified to express a chimeric receptor in which the NK activating receptor NKG2D is fused to the cytotoxic ζ chain of the T cell receptor, called NKG2D.ζ (*12*). We have shown that NKG2D.ζ-bearing NK cells target and eliminate human MDSCs from the TME of solid tumors while sparing normal cells (*12*). We tested NKG2D.ζ NK cells in a TME xenograft model in which co-inoculation of pediatric neuroblastoma (NB) (the most common extracranial solid tumor of childhood) with human MDSCs in immunocompromised NSG mice modeled TME-mediated suppression. We chose NKG2D ligand–negative LAN-1 tumor for this model so that NKG2D.ζ NK cells would only target MDSCs and not tumor cells within the xenografts, thus allowing evaluation of the effects of specifically targeting a component of the TME on tumor parameters. To determine the MDSC dose in our xenograft model that resulted in increased MDSC burden within the TME, we engrafted LAN-1 NB with increasing percentages of MDSCs (Fig. 1A). When tumors became quite large (>1500 mm^3; approximately day 28), they were extracted en bloc and total MDSC burden was enumerated by flow cytometry. As seen in Fig. 1B, there was an inoculation dose-dependent rise in MDSC burden within these advanced tumors. Further, when tumor tissue was examined by immunohistochemistry (IHC) for CD31 [marker for microvessel density (MVD)] and S100A9 (marker for human tissue-resident MDSCs), MDSC-containing tumor sections showed an MDSC dose-dependent increase in MVD and perivascular distribution of MDSCs (Fig. 1C). Furthermore, increasing inoculation doses of MDSCs during tumor engraftment resulted in significantly elevated levels of the circulating human suppressive cytokines interleukin-6 (IL-6), IL-10, and transforming growth factor–β as compared with control tumors without MDSCs (Fig. 1D). To confirm that engraftment of human MDSCs in a dose-dependent manner within the solid tumor TME model resulted in increasing immunosuppression, we examined the ability of GD2 NB antigen-specific CAR-T cells (GD2.CAR-T cells) to mediate tumor regression in mice bearing xenografts containing increasing doses of human MDSCs (Fig. 1E). Whereas GD2.CAR-T cells mediated complete regression of control tumor xenografts without MDSCs, the same doses were ineffective in regressing tumor xenografts containing increasing doses of MDSCs (Fig. 1F). We next wanted to determine whether cellular immunotherapy directed against only the TME (no direct antitumor cell effect) would be similarly inhibited by MDSCs or regress tumor. Increasing doses of MDSC-targeting NKG2D.ζ NK cells (range, 5×10^6 to 1×10^8 cells per animal) were administered to mice bearing NKG2D ligand–negative NB tumors with 50% inoculation dose of human MDSCs (Fig. 1G). The 50% MDSC inoculation dose was chosen for all future experiments, as data from Fig. 1 (C, D, and F) indicated optimal immunosuppression at this dose. Although intratumoral MDSC reduction was achieved after NK cell infusion and was NK cell dose dependent (Fig. 1H), there were only minor changes in tumor size, as determined by caliper-based measurements (Fig. 1I). These results suggest that, in contrast to tumor antigen–directed cellular therapy such as CAR-T cells, where response may be directly gauged via tumor size measurement, response to TME-directed cellular therapy (i.e., intratumoral MDSC elimination) may not correlate directly with changes in tumor size.

MDSCs localize to perivascular intratumoral regions and are eliminated effectively by NKG2D.ζ-modified NK cells

To determine whether global tumor metrics derived from contrast-enhanced imaging would detect changes in tumor produced after TME-directed cellular therapy, we used our MDSC-containing TME xenograft model in a setup similar to the schema in Fig. 1G, this time adding nanoparticle contrast–enhanced imaging on day 28 in addition to ex vivo tumor assessment by flow cytometry and IHC (see schema in Fig. 2A). Analysis of intratumoral MDSC levels using flow cytometry confirmed the efficacy of MDSC-directed NK cell therapy. MDSC levels in the immunotherapy group were significantly lower than those in the untreated group and reached similar levels to the non-MDSC control group (Fig. 2B). Spatial microscopic analysis of IHC revealed a predominant perivascular distribution of MDSCs in both the untreated MDSC-containing tumors and immunotherapy group (Fig. 2C). However, the level of perivascular MDSCs was significantly reduced in tumors that received NK cell immunotherapy (Fig. 2D). CD31 staining of intratumoral blood vessels revealed a higher MVD in untreated MDSC-containing tumors than in control tumors devoid of MDSCs (T) (Fig. 2E). Tumors that received NK cell immunotherapy demonstrated a lower MVD than untreated tumors, indicating reduction in tumor vascularity upon intratumoral MDSC depletion.

Imaging-derived global tumor metrics do not correlate with intratumoral MDSC depletion

Imaging-derived global tumor metrics were computed to determine whether these parameters can be prognostic for changes in the TME after MDSC-depleting therapy. Nanoparticle contrast–enhanced CT-derived tumor volumes in mice bearing MDSC-containing tumors that received NK immunotherapy (T + M + Tx, 3.61 ± 1.10 cm^3) were not significantly different compared with MDSC-containing untreated tumors (T + M, 2.27 ± 1.13 cm^3) and control tumors devoid of MDSCs (T, 2.38 ± 0.93 cm^3) (Fig. 3A). CT-derived tumor attenuation on nanoparticle contrast–enhanced delayed CT scans, an indicator of tumor vascular leakiness, did not differ between immunotherapy (400 ± 12 HU), untreated (410 ± 13 HU), and control

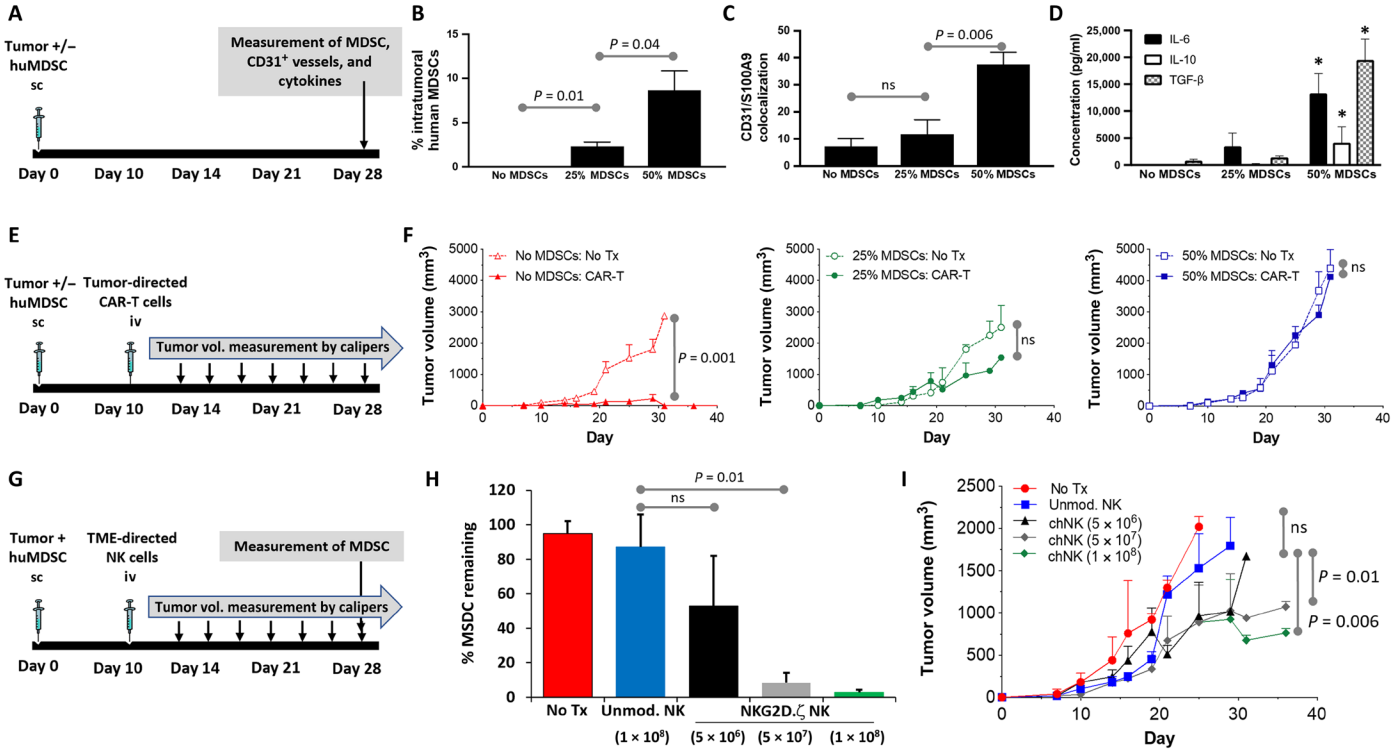

Fig. 1. Elimination of intratumoral MDSCs does not correlate with tumor regression. (**A**) Treatment schema for experiments assessing MDSC dose-dependent tumor burden, vessel density, and suppressive environment. (**B**) Tumors were harvested en bloc, and percentage of MDSCs within tumors inoculated alone (No MDSCs) or with a 25 or 50% MDSC inoculation dose was determined by flow cytometry. (**C**) Tumors were harvested, sectioned, and analyzed ($n = 5$ samples per section) for presence of microvasculature by human CD31 immunostaining and of human MDSCs by S100A9 immunostaining on hematoxylin and eosin (H&E) of tissue sections. Shown is number of areas where MDSCs and CD31 vessels colocalize within tumors inoculated alone (No MDSCs) or with a 25 or 50% MDSC inoculation dose. (**D**) Levels of suppressive cytokines in serum of mice with tumors alone or inoculated with 25 or 50% MDSC dose. * indicates $P < 0.05$ vs. same cytokine in other groups. (**E**) Treatment schema for experiments assessing MDSC dose-dependent immunosuppression. (**F**) Neuroblastoma antigen GD2-specific CAR-T cells were injected into mice bearing tumor xenograft alone (No MDSCs) or mice bearing xenografts containing 25 or 50% MDSC dose, and tumor volume was followed over time. Control mice received non-CAR modified T cells (no Tx). (**G**) Treatment schema for experiments assessing effect of MDSC-targeting NKG2D.ζ-modified NK cells on (**H**) intratumoral MDSCs and (**I**) tumor volume. ns, not significant; sc, subcutaneously; iv, intravenously.

groups (402 ± 13 HU) (Fig. 3B). Tumor fractional blood volume, an indicator of tumor vascularity, did not change significantly in the immunotherapy group (5.1 ± 1.7%) compared with the untreated (9.6 ± 7.8%) and control groups (5.3 ± 2.8%) (Fig. 3C). Nanoparticle contrast–enhanced delayed CT imaging demonstrated heterogeneous spatial patterns of intratumoral signal enhancement due to the accumulation of nanoparticle contrast agent at sites of increased vascular permeability in tumors of all groups (Fig. 4). Nanoparticle contrast–enhanced CT angiography demonstrated presence of sporadic large vessels in the central region of MDSC-containing tumors in the untreated group (T + M) compared with the immunotherapy and control groups devoid of MDSCs. Similarly, noncontrast T2-weighted magnetic resonance (T2w-MR) also indicated heterogeneous contrast pattern in MDSC-containing untreated tumors (T + M) compared with immunotherapy and control groups devoid of MDSCs (fig. S2).

Nano-radiomic features correlate with tumor changes after intratumoral MDSC depletion mediated by TME-directed cellular immunotherapy

To determine whether advanced quantitative imaging can be prognostic for changes in the TME after MDSC-depleting therapy, so as to circumvent reliance on conventional imaging metrics such as tumor size, radiomic analysis was performed on segmented tumor volumes generated from nanoparticle contrast–enhanced delayed CT, CT angio, and noncontrast T2w-MR images. A total of 107 radiomic features (RFs) were computed for each segmented tumor volume obtained from each imaging methodology. To eliminate potential for bias, shape- and size-based radiomic features were excluded because tumors in the immunotherapy group showed, although not statistically significant, larger tumor size compared with the untreated and control groups. As a result, 91 of 107 RFs were investigated for their discriminatory power in differentiating the immunotherapy group from the untreated group. Tumors from the untreated group demonstrated high correlation among RFs than tumors from the immunotherapy group, analyzed by all three imaging methodologies (Fig. 4). Nano-radiomic analysis revealed 10 RFs based on nanoparticle contrast–enhanced delayed CT leak datasets and 13 features based on nanoparticle contrast–enhanced CT angiographic datasets that were able to statistically differentiate ($P < 0.05$) the immunotherapy and untreated groups (Table 1). In comparison, radiomic analysis of noncontrast T2w-MR images identified five features that statistically differentiated ($P < 0.05$) the immunotherapy and untreated groups. Texture-based RFs belonging to gray level size zone matrix (GLSZM) class and gray level run length matrix (GLRLM) were among the predominant features exhibiting high statistical power in differentiating the immunotherapy group from the untreated group

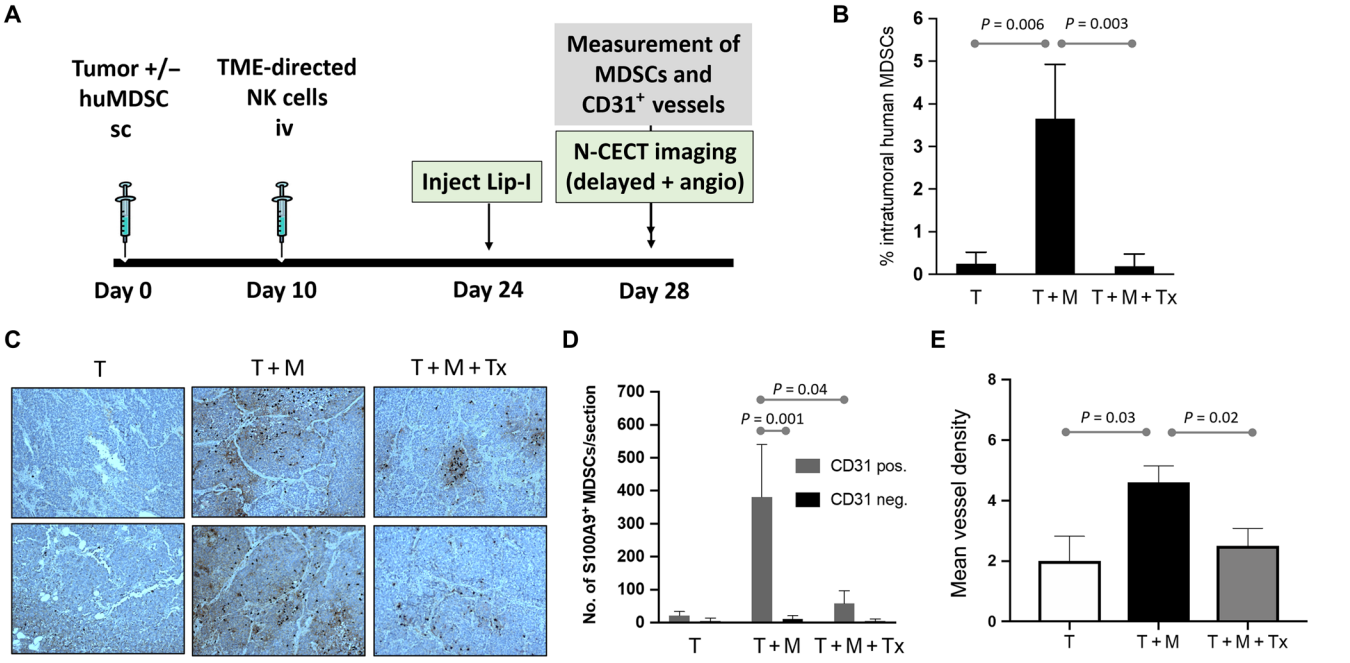

Fig. 2. Intratumoral MDSCs localize to areas of high CD31 vessel density and are eliminated effectively by NKG2D.ζ-modified NK cells. (**A**) Experimental schema for evaluating changes in MDSC burden after TME-directed NK cell therapy by flow cytometry, IHC, and nanoparticle contrast–enhanced CT imaging. (**B**) Intratumoral MDSC burden in tumor-only (T), tumor + MDSC (T + M), and tumor + MDSC + NK cell immunotherapy (T + M + Tx) groups was quantified per group by flow cytometry for $CD14^+$/HLA-DR^{neg}/intracellular $S100A9^+$ cells. (**C**) Tumors were harvested, sectioned, and analyzed ($n = 5$ samples per section) for presence of microvasculature by human CD31 immunostaining (brownish red) and of human MDSCs by S100A9 immunostaining (black) on H&E of tissue sections. Shown are two representative sections of tumors inoculated without (T) or with MDSCs (T + M) and tumors with MDSCs after NK cell immunotherapy (T + M + Tx). (**D**) Number of $S100A9^+$ MDSCs within areas of each tumor section containing $CD31^+$ vessels (CD31 positive) were enumerated and compared to MDSC numbers in areas devoid of $CD31^+$ vessels (CD31 negative). (**E**) MVD analysis demonstrates a reduction in tumor vascularity after depletion of MDSCs in the NK cell therapy group. Data are presented as means ± SEM ($n = 9$ to 10 animals per group).

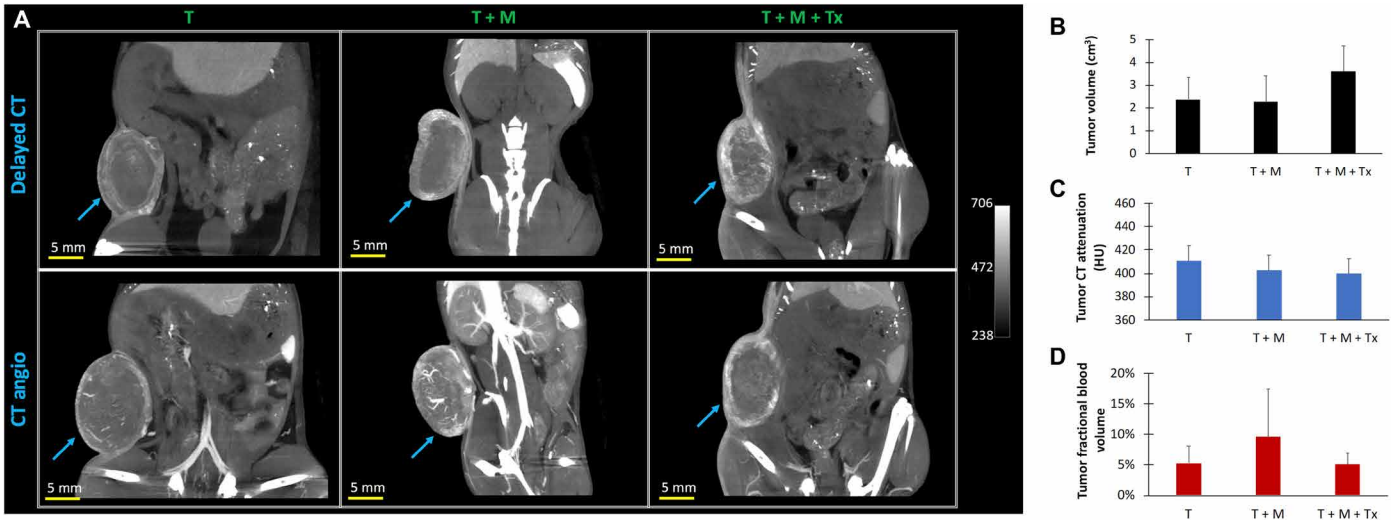

Fig. 3. Nanoparticle contrast–enhanced CT imaging. (**A**) Representative thick slab coronal images of mouse lower abdomen showing tumor signal enhancement on delayed CT image (top row) and CT angio image (bottom row) for an animal in the tumor-only control group (T, left column), tumor + MDSC untreated group (T + M, middle column), and tumor + MDSC + NK cell immunotherapy group (T + M + Tx, right column). Delayed CT images were acquired 4 days after administration of nanoparticle contrast agent. Immediately thereafter, a second dose of nanoparticle contrast agent was injected to acquire CT angiography within an hour after contrast administration. (**B**) CT-derived tumor volume, (**C**) CT-derived mean tumor attenuation [Hounsfield units (HU)], from delayed CT scan due to accumulation of nanoparticle contrast agent, an indicator of tumor vascular permeability and tumor leakiness, and (**D**) CT-derived mean tumor fractional blood volume, an indicator of tumor vascularity, in tumors alone (T), tumor inoculated with human MDSCs (T + M), and tumors with MDSCs after NK cell therapy (T + M + Tx). CT-derived global tumor metrics did not show significant group differences ($P > 0.05$). Data are presented as means ± SD ($n = 9$ to 10 animals per group).

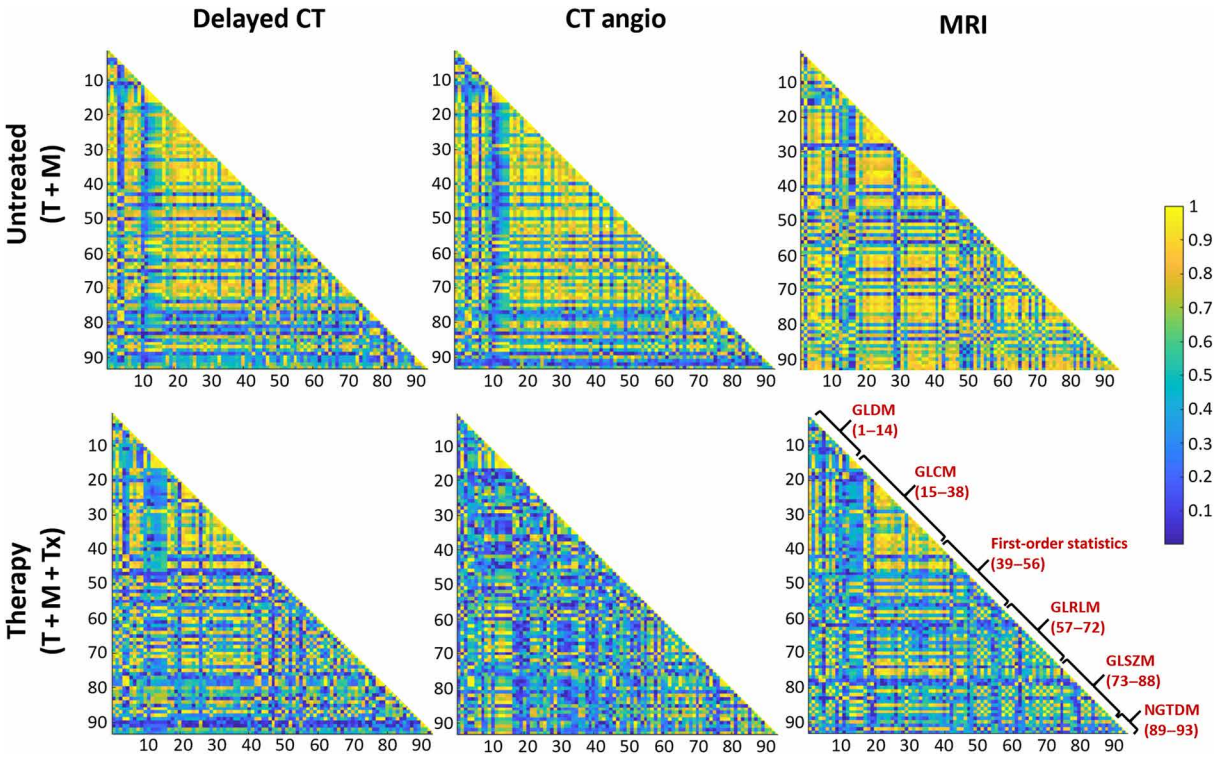

Fig. 4. Radiomic feature maps. Correlation matrix maps of radiomic features generated from analysis of nanoparticle contrast–enhanced delayed CT and CT angio and noncontrast MRI. Maps are presented for the tumor + MDSC untreated group (T + M, top row) and tumor + MDSC + NK cell therapy group (T + M + Tx, bottom row). GLCM, gray level co-occurrence matrix; GLDM, gray level dependence matrix; NGTDM, neighboring gray tone difference matrix.

Table 1. Radiomics-based differentiation of immunotherapy-treated tumors and untreated tumors. Number of radiomic features under each class that differentiated ($P < 0.05$) the immunotherapy group (T + M + Tx) and untreated group (T + M). Radiomic analysis was performed on nanoparticle contrast–enhanced delayed CT, CT angio, and noncontrast T2-weighted MR images.

Radiomic feature class	CT delayed	CT angio	T2w MRI
First-order statistics	0	2	1
Gray level co-occurrence matrix (GLCM)	0	0	1
Gray level dependence matrix (GLDM)	2	2	1
Gray level run length matrix (GLRLM)	2	2	1
Gray level size zone matrix (GLSZM)	5	6	1
Neighboring gray tone difference matrix (NGTDM)	1	1	0

(Fig. 5). Some of the RFs demonstrated significant differences between the therapy and control (tumor only) groups. A complete list of RFs demonstrating significant difference between the immunotherapy and untreated groups is provided in tables S1 to S3.

DISCUSSION

TME-directed cellular immunotherapies are undergoing preclinical and clinical development (*15*). These use live engineered cells that adapt to changing conditions so that they may survive, home, extravasate, and traffic to key intratumoral sites, all while maintaining antitumor effector functions and therefore are distinctly different from checkpoint blockade immunotherapies. Because of the indirect and often delayed effects of TME-targeting strategies on tumor growth, advanced imaging methods that enable detection of response to these therapies would play an important role in patient management. In this preclinical study, we investigated a nano-radiomics approach for identifying quantitative imaging features within a tumor indicative of phenotypic changes after TME-directed cellular immunotherapy. In a TME xenograft model comprising human MDSCs, we show that response to MDSC-directed cellular immunotherapy did not correlate with changes in imaging-derived tumor size, a standard clinical metric for disease evaluation. In contrast, radiomic analysis performed on segmented tumor volumes generated from nanoparticle contrast–enhanced delayed CT, CT angio, and noncontrast T2w-MR images revealed RFs that correlated with tumor changes after intratumoral MDSC-depleting cellular immunotherapy.

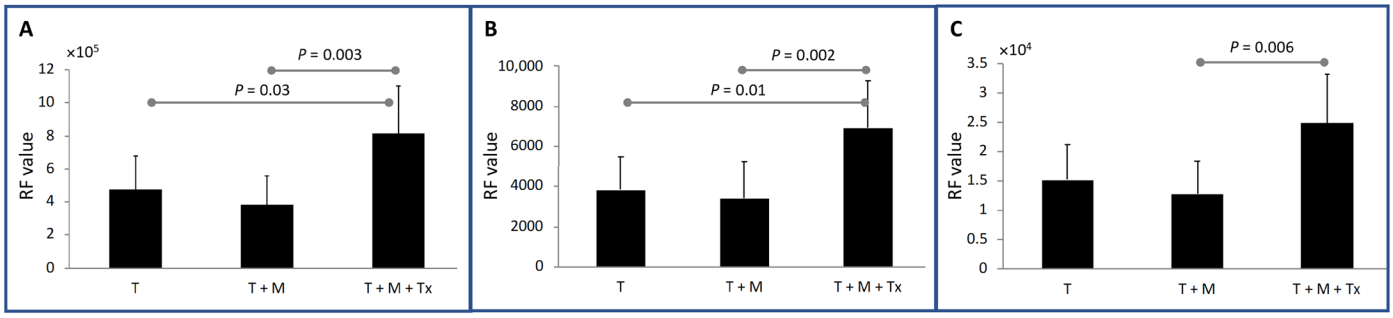

Fig. 5. Radiomic features differentiate immunotherapy-treated tumors and untreated tumor. Examples of radiomic features differentiating the untreated group (T + M) from the immunotherapy group (T + M + Tx) for (**A**) delayed CT images analyzed using GLRLM run length nonuniformity RF, (**B**) CT angio images analyzed using GLSZM gray level nonuniformity RF, and (**C**) noncontrast T2w-MR images analyzed using GLRLM run length nonuniformity RF.

We used a clinically relevant human xenograft TME model in NSG mice wherein human tumor cells grow in the presence of human suppressive immune cells (*12*). Physical cell-cell interactions play a critical role in generating an immunosuppressive microenvironment in solid tumors (*16*). Several adult and pediatric solid tumors, including clinical NB, contain intense infiltrates of MDSCs (*17*), which should be included in tumor xenograft models used to study human cell therapeutics. Although NSG mice lack a complete immune system in which to examine the effects of multiple endogenous immune components, our ability to engraft human MDSCs within our TME model provides the possibility of simulating immunosuppressive aspects of the solid TME as well as direct testing of human cell therapies that are being developed for clinical trials. These human cellular therapies cannot be tested directly in immune competent mouse models due to differences in targeting epitopes between mouse and human as well as issues with xenorejection. Compared with immune competent tumor models, where the complexity of the TME is often unpredictable, our model allows isolation and perturbation of single variables and direct evaluation of their consequences on tumor response. Further, by varying the tumor burden of suppressive immune cells (i.e., MDSCs), the model enables "fine-tuning" of TME immunosuppression, thereby allowing us to understand the effect of each TME component on tumor response to engineered cellular immunotherapies that are being developed for clinical trials. As proof of principle for the human MDSC dependence of our xenograft microenvironment, we showed that increasing the dose of MDSCs in tumor xenografts increased intratumoral MDSC burden, immunosuppressive cytokine milieu, and vascular density. In addition, increasing the dose of MDSCs in tumor xenografts led to an MDSC dose-dependent inhibition of tumor antigen–directed CAR-T cell activity, thus simulating the treatment-resistant clinical phenotype of solid tumors (*18*, *19*).

In addition to simulating treatment resistance to cell therapy, our model also recapitulates the clinical condition in which response to a therapy directed specifically against cellular players of the TME is not necessarily reflected in the standard clinical tumor evaluation metric: change in overall tumor volume. We show that despite almost complete depletion of intratumoral MDSCs by TME-targeting NK cell immunotherapy, changes in gross tumor volume were minimal. These data are consistent with previous clinical reports showing that changes in tumor size do not accurately capture responses to immune-based therapies in which effects on tumor volume are often indirect or delayed (*8*, *9*). For example, Wolchok *et al.* (*20*) reported that response to checkpoint blockade treatment with single-agent ipilimumab was associated with initial decrease in tumor size in only 10% of patients and that many patients with eventual response failed to exhibit initial decreases. It is now evident in the field of immunotherapy that Response Evaluation Criteria in Solid Tumors (RECIST) or World Health Organization criteria, designed to detect early effects of cytotoxic agents, do not provide accurate assessment of response to immunotherapeutic agents. Further, despite recent attempts at defining specific criteria for the evaluation of antitumor responses within the context of immunotherapeutic agents such as checkpoint blockade antibodies or immune-directed small-molecule inhibitors (immune-related RECIST), it remains difficult to apply these modified criteria directly to cellular immunotherapy (*20*). Cellular immunotherapies (such as CAR-T or CAR-NK cells) are "living drugs" modified with targeting receptors that not only enable them to sense, seek, and destroy cancer cells with specificity but also have secondary effects such as coordination and expansion of immune responses (*21*). Conventional imaging-derived standard tumor metrics present challenges in assessing treatment efficacy in the context of cell-based immunotherapies, especially those directed at the TME. Thus, our attempt at an advanced quantitative imaging methodology represents an important initial step in addressing this unique problem.

Because MDSCs play a central role in tumor angiogenesis and reside in perivascular niches with a TME, we hypothesized that depletion of intratumoral MDSCs will alter tumor vascular architecture and, therefore, tumor texture. Thus, a long circulating nanoparticle blood-pool contrast agent that enables interrogation of tumor vasculature was used, in combination with high-resolution CT imaging, to assess response to MDSC-directed immunotherapy. The long blood-circulating property of liposomal-iodine (Lip-I) nanoparticle contrast agent allowed 3D maps of the tumor's vascular compartment during the blood pool phase when imaged within a few hours after administration of contrast agent (*22*). In addition, because nanoparticles gradually extravasate (over a period of days) at sites of increased vascular permeability and reside in perivascular tumor regions for prolonged periods, delayed contrast-enhanced CT images provide 3D tumor maps of regions with high vascular permeability, indicated by high signal intensity voxels, thus allowing the interrogation of tumor "leakiness" (*13*, *14*). Similar approaches have previously been used to study the effect of tumor vasculature–modulating therapies, differentiate malignant from benign lesions, and 3D mapping of nanoparticle distribution in tumors (*13*, *23*, *24*). Furthermore, delayed imaging with a nanoparticle contrast agent accurately

captures vascular architectural changes in tumors that are less prone to artifacts associated with rapid wash-in/wash-out kinetics and bolus injection/tracking protocols used with conventional small-molecule contrast agents.

Our data confirmed that whole-tumor global CT metrics, even when using a nanoparticle contrast agent that uses aspects of MDSC biology, are insensitive to the indirect subtle changes associated with TME-directed therapies. As demonstrated by flow cytometry, tumors in the immunotherapy group exhibited significantly lower MDSC burden compared with the untreated group, consistent with our previous observations demonstrating efficacy of MDSC-directed NK cell therapy (*12*). Furthermore, immunohistochemical analysis indicated a significant reduction in MVD in the immunotherapy group compared with the untreated group. However, global tumor metrics on CT imaging (overall volume, CT attenuation, and fractional blood volume) did not corroborate with findings of NK cell immunotherapy efficacy (i.e., intratumoral MDSC depletion). Although previous studies have attempted to define noninvasive radiomic biomarkers in the context of checkpoint blockade and tyrosine kinase inhibitors, our study is the first to evaluate nanoparticle contrast–based imaging in the assessment of tumor changes after cellular immunotherapy, especially one that specifically targets the TME. Further, our data underscore the need for advanced analytics in correlating efficacy with tumor changes.

Radiomic analysis was performed on high-resolution nanoparticle contrast–enhanced CT images. In addition, radiomic analysis was performed on noncontrast T2w-MR images, which provides native contrast, and has potential for clinical translation because patients with cancer routinely undergo noncontrast MRI for monitoring of treatment response. Analysis of nanoparticle contrast–enhanced delayed CT and CT angiograms (CTAs) revealed several RFs that enabled detection of early response to NK cell therapy, i.e., differentiation of the immunotherapy group from the untreated group. These findings suggest that TME-directed immunotherapy induces subtle changes in the tumor architecture that may not be detectable using global tumor imaging metrics but can be detected by quantitative nano-radiomic analysis that involves data mining of high-resolution 3D images. Radiomic analysis of T2w-MR images also revealed RFs, albeit with fewer number of features when compared with features identified from the analysis of nanoparticle contrast–enhanced CT images, for the detection of treatment response. Texture-based RFs belonging to GLSZM and GLRLM exhibited the highest discriminatory power for the detection of tumor response to MDSC-directed therapies. GLSZM is a class of texture features that quantifies gray level zones, which is defined as the number of connected voxels with similar intensity levels, within images (*11*). For instance, GLSZM nonuniformity feature evaluates homogeneity in gray level intensities between zones. A higher value indicates a higher degree of heterogeneity in gray level zones. GLRLM is another class of texture features that quantifies path length of connected voxels that exhibit similar gray level intensities (*11*). It is likely that depletion of MDSCs by NK cell therapy reduces tumor vascularity, as demonstrated by IHC, which reflects as a heterogeneous pattern of signal intensities on nanoparticle contrast–enhanced CT images. Analysis of these features suggests that immunotherapy-driven MDSC depletion results in a high degree of tumor texture heterogeneity. A high correlation was observed between RFs in 3D image maps from the MDSC-containing untreated group, indicating a higher uniform tumor spatial representation when compared with 3D image maps from the immunotherapy group. The low inter-RF correlation in the immunotherapy group could indicate a vast spread of architectural changes, and therefore high texture heterogeneity, in response to TME-directed NK cell therapy. Radiomic analysis of CT images has the advantage of providing rich information by using high spatial resolution imaging. Furthermore, ease of imaging standardization provides additional benefits for reproducible quantitative imaging using this modality (*25*). Radiomic analysis of contrast-enhanced CT images has been used to assess intratumoral burden of CD8 cells and response to anti–PD-1 (programmed cell death protein 1) checkpoint blockade immunotherapy (*26*, *27*). Furthermore, texture-based RFs have demonstrated strong discriminatory power in the prediction of treatment response to a variety of therapies (*28*, *29*).

Our work is important for two main reasons. First, this is the first study applying radiomic analysis to cellular immunotherapies, which are distinctly different from checkpoint blockades and will soon enter clinical trials for treatment of pediatric solid tumors. Furthermore, by using a clinically validated radiomic software, to noninvasively determine image-based quantitative phenotypic features indicative of tumor response to TME-directed cellular immunotherapies, we show its applicability and high potential for clinical translation for treatment response monitoring in the emerging field of cell-based cancer therapies. We believe that radiomics will be immensely useful in the clinic in determining tumor response to next-generation immunotherapies, including cellular immunotherapies, due to substantial heterogeneity in treatment response and the high cost associated with "living" cell-based therapies. Second, our work is the first application of radiomics to nanoparticle contrast–enhanced imaging. Unlike molecular contrast agents, tumor accumulation and intratumoral distribution of nanoparticle contrast agent is predominantly a function of tumor architecture. Furthermore, extravasated NP contrast agent resides in tumor for prolonged period and therefore eliminates the introduction of confounding variables in radiomic analysis that may be present in conventional molecular-based contrast-enhanced images such as dose and rate of contrast administration, bolus timing, and image acquisition, which can affect reproducibility of RFs.

We acknowledge that our study has limitations. Since CT and MR imaging sequences provide a high degree of flexibility with respect to scan parameters, the effect of changes in scan parameters on the robustness of RFs requires further investigation (*25*). The predictive power of RFs on tumor response to anticancer therapies has not been evaluated in our study. Radiomic analysis was not performed on non–contrast-enhanced CT images due to absence of 3D signal intensity variations in noncontrast CT images. In general, radiomics approaches analyze variations in pattern of signal intensities and tissue texture to extract phenotypic and tissue architectural differences. Absence of signal intensity variations is unlikely to yield RFs indicative of treatment response or tumor phenotype. Exceptions would be spontaneous and orthotopic lesions wherein the signal intensities of tumor boundaries differ substantial from surrounding normal tissue, such as lung cancer. Future studies will build on the promising results of this work to determine the sensitivity and specificity of the RFs in tumor response to combinatorial (antitumor + TME-directed) immunotherapies. Future studies are also warranted to validate RFs in other tumor models, such as sarcoma, where TME-directed cellular therapies in combination with antitumor T cell immunotherapy are undergoing preclinical investigations (*15*). Although, we used a Lip-I nanoparticle contrast agent in combination with

high-resolution CT, it is possible that, because of rapid imaging speed of clinical CT, radiomic analysis of contrast-enhanced CT images obtained using conventional molecular CT contrast agents could yield phenotypic features indicative of treatment efficacy for TME-directed cellular immunotherapies, thus increasing potential for rapid clinical translation of such approaches. In addition, radiomic investigations can be performed in contrast-enhanced MR images acquired using ultrasmall iron oxide nanoparticles, which are being investigated for monitoring burden of intratumoral immune cells in clinical trials (*30*).

In conclusion, our study describes a preclinical approach for the application of nano-radiomic analysis in the field of cellular immunotherapy. These disciplines have been combined to help further understand efficacy of cellular immunotherapy in harsh solid TMEs. Current attempts in our laboratory at multiparametric optimization of imaging methodologies and sequences in the preclinical domain to enable the selection of the most promising imaging techniques for clinical translation would serve to implement radiomic analysis for monitoring response to cellular immunotherapies.

MATERIALS AND METHODS

Cell lines and cytokines

The human NB cell line LAN-1 was purchased from the American Type Culture Collection (ATCC) (Manassas, VA, USA) and cultured in DMEM (Dulbecco's modified Eagle's medium) culture medium supplemented with 2 mM L-glutamine (Gibco-BRL) and 10% fetal bovine serum (FBS) (Hyclone, Waltham, MA, USA). A modified version of parental K562 cells, genetically modified to express a membrane-bound version of IL-15 and 41BB-ligand, K562-mb15-41BB-L, was provided by D. Campana (National University of Singapore). All cell lines were verified by either genetic or flow cytometry–based methods (LAN-1 authenticated by ATCC in 2011) and tested for mycoplasma contamination monthly via MycoAlert (Lonza) mycoplasma enzyme detection kit (last mycoplasma testing of LAN-1 and K562-mb15-41BB-L on 8 October 2019; both negative). All cell lines were used within 1 month of thawing from early-passage (<5 passages of original vial) lots. Recombinant human IL-2 was obtained from the National Cancer Institute Biologic Resources Branch (Frederick, MD). Recombinant human IL-6, GM-CSF (granulocyte-macrophage colony-stimulating factor), IL-7, and IL-15 were purchased from PeproTech (Rocky Hill, NJ, USA).

CAR-encoding retroviral vectors

The construction of the SFG-retroviral vector encoding GD2-CAR. 41BB.ζ was described (*31*). The SFG-retroviral vector encoding NKG2D.ζ, an internal ribosomal entry site (IRES), and truncated CD19 (tCD19), was generated by subcloning NKG2D.ζ from a retroviral vector (*32*), provided by C. L. Sentman (Dartmouth Geisel School of Medicine, Hanover, NH, USA), into pSFG.IRES.tCD19 (*33*). RD114-pseudotyped viral particles were produced by transient transfection in 293T cells, as previously described (*34*).

Expansion and retroviral transduction of human NK and T cells

Human NK cells were activated, transduced with retroviral constructs, and expanded as previously described by our laboratory (*35*). Briefly, peripheral blood mononuclear cells (PBMCs) obtained from healthy donors under Baylor College of Medicine IRB–approved protocols were cocultured with irradiated (100 Gy) K562-mb15-41BB-L at a 1:10 (NK cell:irradiated tumor cell) ratio in G-Rex cell culture devices (Wilson Wolf, St. Paul, MN, USA) for 4 days in Stem Cell Growth Medium (CellGenix) supplemented with 10% FBS and IL-2 (500 IU/ml). Cell suspensions on day 4 (containing 50 to 70% expanded/activated NK cells) were transduced with SFG-based retroviral vectors, as previously described (*36*). The transduced cell population was then subjected to secondary expansion to generate adequate cell numbers for in vivo experiments in G-Rex devices at the same NK cell:irradiated tumor cell ratio with IL-2 (100 IU/ml). This 17-day human gene-modified NK cell protocol resulted in >95% pure $CD56^+/CD3^-$ NK cell population with an average of 72.1 ± 10.1% (n = 5) of NK cells transduced with the construct of interest. For most experiments, transduced NK cells were purified to >90% by magnetic column selection of tCD19 selection marker–positive cells. For the production of GD2.CAR-T cells (autologous to MDSCs), PBMCs from healthy donors were suspended in T cell medium consisting of RPMI 1640 supplemented with 45% Click's Medium (Gibco-BRL), 10% FBS, and 2 mM L-glutamine and cultured in wells precoated with CD3 (OKT3, CRL-8001, ATCC) and CD28 (Clone CD28.2, BD Biosciences) antibodies for activation. Human IL-15 and IL-7 were added on day +1, and cells underwent retroviral transduction on day +3, as previously described (*36*). T cells were used for experiments between days +10 and +14 after transduction, with phenotype as reported previously (*12*).

Induction and enrichment of human MDSCs

Our method for ex vivo enrichment of human PBMC-derived MDSCs was derived from published reports (*37*), with slight modifications. Briefly, PBMCs were sequentially depleted of $CD25^{hi}$-expressing cells and CD3-expressing cells by magnetic column separation (Miltenyi Biotec). Resultant $CD25^{lo/-}$, $CD3^-$ PBMCs were plated at 4×10^6 cells/ml in complete RPMI medium with human IL-6 and GM-CSF (both at 20 ng/ml) onto 24-well culture plates (Sigma Corning) at 1 ml per well. Plates were incubated for 7 days with medium, and cytokines were replenished on days 3 and 5. Resultant cells were harvested by gentle scraping, and MDSCs were purified by magnetic selection using CD33 magnetic microbeads (Miltenyi Biotec). Cells were analyzed by multicolor flow cytometry for CD33, CD14, CD15, HLA-DR, CD11b, CD83, and CD163 (BD Biosciences). MDSCs were defined as either monocytic (M-MDSCs; $CD14^+$, $HLA\text{-}DR^{low/-}$), polymorphonuclear (PMN)–MDSCs ($CD14^-$, $CD15^+$, $CD11b^+$), or early-stage MDSCs ($lineage^-$, $HLA\text{-}DR^{low/-}$, $CD33^+$), as per published guidelines (*38*).

TME xenograft model and treatments

We recently described the development of a preclinical xenograft model that simulates the treatment-resistant clinical phenotype of immunosuppressive solid tumors to study efficacy of cellular immunotherapies (*12*). On day 1, 12- to 16-week-old female NSG mice were randomized to three treatment groups (n = 5 per group, performed in replicates, total n = 10 per group). Animals in the non-MDSC tumor-only control group (T group) were subcutaneously implanted with 1×10^6 LAN-1 NB tumor cells in the dorsal right flank. Animals in the tumor + MDSC untreated group (T + M group) and the tumor + MDSC + NK cell immunotherapy group (T + M + Tx group) were implanted with 1×10^6 LAN-1 NB tumor cells admixed with varying doses of MDSCs (none, 25, or 50% of the tumor cell dose). Cells were suspended in 100 μl of basement membrane Matrigel

(Corning) to keep tumor cells and MDSCs confined so as to establish a localized solid TME. Tumor growth was measured twice weekly by caliper measurements. For model characterization experiments, on day 28, percentage of intratumoral MDSCs was quantified by flow cytometry, MDSC colocalization to microvasculature by IHC, and serum human cytokines levels by enzyme-linked immunosorbent assay, as described below. For CAR-T cell immunosuppression experiments, 5 $\times 10^6$ human GD2.CAR-T cells were injected intravenously on day 10 following tumor xenograft implantation. For TME-directed NK cell experiments, on day 10 when tumors reached approximately 100 mm^3, animals in the T + M + Tx group received a single intravenous injection of 1×10^7 MDSC-targeting NKG2D.ζ NK cells followed by 500 IU per mouse IL-2 given intraperitoneally every other day for six total doses to promote NK cell survival (*39*). On day 24, animals in all groups received an intravenous injection of Lip-I nanoparticle CT contrast agent (1.1 g I/kg). On day 28, 4 days after administration of the Lip-I contrast agent, delayed CT imaging was performed to assess tumor leakiness. Immediately thereafter on the same day, a second dose of Lip-I contrast agent (1.1 g I/kg) was administered for acquiring a CTA. Subsequently, the animals underwent noncontrast MRI. The animals were euthanized after the final imaging session on day 28, and tumors were harvested for postmortem analysis. If necessary, mice were euthanized for excessive tumor burden, as per protocol guidelines. The animal study protocol was approved by Baylor College of Medicine Institutional Animal Care and Use Committee, and mice were treated in accordance with the institutional guidelines for animal care.

Nanoparticle contrast agent

A Lip-I nanoparticle contrast agent was used for nanoparticle contrast–enhanced CT imaging (*13*). The contrast agent was fabricated by dissolving 1,2-dipalmitoyl-sn-glycero-3-phospho-choline, cholesterol, and 1,2-distearoyl-sn-glycero-3-phosphoethanolamine-*N*-[methoxy (polyethylene glycol)-2000] in ethanol at a molar ratio of 56:40:4. An aqueous solution of iodixanol (550 mg I/ml) was added to the lipid solution and hydrated for 30 min followed by sequential extrusion at ~65°C. The extruded liposomal nanoparticle solution was diafiltered against 150 mM saline solution/10 mM histidine to remove unencapsulated iodixanol. The average liposome size in the final formulation, determined by dynamic light scattering, was 138 ± 23 nm. The iodine concentration, determined by ultraviolet spectrophometry ($\lambda_{245\,nm}$), was 110 ± 8 mg I/ml.

Nanoparticle contrast–enhanced CT

CT imaging was performed on a small animal micro-CT scanner (Inveon, Siemens Inc., Knoxville, TN, USA). Animals were anesthetized using 3 to 4% isoflurane, positioned on the CT cradle, and then maintained at 1 to 1.5% isoflurane delivered via a nose cone. Respiratory rate was monitored by a pneumatic pressure pad placed underneath the animal. Animals underwent two types of CT scans. A delayed CT was performed 4 days after injection of Lip-I contrast agent (1.1 g I/kg) to capture 3D maps of tumor vascular leakiness (*13*). Immediately thereafter, a second dose of Lip-I contrast agent (1.1 g I/kg) was administered to capture 3D maps of tumor angiogram. Lip-I contrast agent was fabricated in-house as per methods described previously (*13*). CT images were acquired using the following scan parameters: 70 kVp, 0.5 mA, 850-ms x-ray exposure, 540 projections, ~20-min scan time (*13*). Images were reconstructed by filtered back-projection at an isotropic resolution of 35 μm and calibrated for Hounsfield units (HU).

Magnetic resonance imaging

Imaging was performed on a 1-T permanent MRI scanner (M2 system, Aspect Imaging, Shoham, Israel). A 60-mm volume coil was used for transmission and reception of RF signal. Animals were sedated using 3 to 4% isoflurane, set up on the MRI animal bed, and then maintained at 1 to 1.5% isoflurane delivered using a nose cone setup. Respiratory rate was monitored by a pneumatically controlled pressure pad placed underneath the abdominal region of the animals. Noncontrast T2w images were acquired using a fast spin echo (FSE) sequence. Scan parameters for the T2w-FSE sequence were as follows: echo time (TE) = 80 ms, repetition time (TR) = 6816 ms, slice thickness = 0.8 mm, field of view = 80 mm, number of slices = 38, matrix = 256 × 250, acquisition plane = coronal, in-plane resolution = 320 × 320 μm^2, number of excitations = 2, and scan time = ~6 min.

Image and radiomic analysis

Regions of interest (ROIs) were manually drawn in CT and MR images to delineate tumor margins for 3D segmentation of tumor volume. Global image-derived CT metrics were computed for segmented tumors. These included tumor volume and tumor CT attenuation in delayed CT (CTD) and CTA scans. Tumor fractional blood volume was determined as [Tumor CT $attenuation_{CTA}$ − Tumor CT $attenuation_{CTD}$]/[Blood CT $attenuation_{CTA}$ − Blood CT $attenuation_{CTD}$], wherein CTA and CTD refers to CT angiogram and delayed CT scans (*40*). ROIs drawn in the inferior vena cava was used for CT attenuation in blood. Group values were reported as means ± SD. Radiomic analysis was performed using an open-source software (PyRadiomics) containing a total of 107 RFs to analyze shape, size, intensity, morphology, and texture (*11*). These RFs were categorized into the following five classes: first-order statistics, shape descriptors, and texture classes that include gray level co-occurrence matrix (GLCM), GLRLM, GLSZM, gray level dependence matrix (GLDM), and neighboring gray tone difference matrix (NGTDM). Radiomic features were computed for segmented tumors generated from noncontrast T2w-MR, nanoparticle contrast–enhanced delayed CT, and CT angiographic images.

Flow cytometry

At the end of the experiments, tumors were harvested en bloc, digested ex vivo, and intratumoral human MDSCs ($CD33^+$, $HLA\text{-}DR^{low}$ cells) were enumerated by flow cytometry using commercially available antibodies from BD Biosciences, as previously reported (*12*). In some experiments, the absolute number of human MDSCs within a tumor digest was enumerated per mouse (n = 5 mice per group), compared with pretreatment MDSC numbers, and presented as mean % MDSCs remaining per treatment group.

Immunohistochemistry and microscopic analysis

On day 28, tumors were harvested, sectioned, and n = 5 samples per section were analyzed for presence of microvasculature by hematoxylin and eosin and human CD31 immunostaining (Abcam, San Francisco, CA, USA) and human MDSCs by S100A9 immunostaining (Abcam, San Francisco, CA, USA). Tissue processing and immunohistochemical staining were performed by the Human Tissue Acquisition and Pathology Core of Baylor College of Medicine. The number of $S100A9^+$ MDSCs within areas of each tumor section containing $CD31^+$ vessels were enumerated and compared to MDSC numbers in areas devoid of $CD31^+$ vessels by counting 10 different representative high-powered fields at ×40 magnification per section per tumor.

Statistical analysis

Nonimaging data are presented as means ± SEM of either experimental replicates or number of donors, as indicated. Paired two-tailed *t* test was used to determine significance of differences between means, with $P < 0.05$ indicating a significant difference. Multiple group comparisons for in vivo studies were conducted by analysis of variance (ANOVA) via GraphPad Prism v7 software. Global nanoparticle contrast–enhanced CT-derived metrics and selection of RFs were performed using a Kruskal-Wallis test with Bonferroni correction for multiple intergroup comparisons. A P value <0.05 was considered statistically significant. 2D maps were generated to present pairwise linear correlation coefficient between RFs.

SUPPLEMENTARY MATERIALS

Supplementary material for this article is available at http://advances.sciencemag.org/cgi/content/full/6/28/eaba6156/DC1

View/request a protocol for this paper from *Bio-protocol*.

REFERENCES AND NOTES

1. S. L. Maude, N. Frey, P. A. Shaw, R. Aplenc, D. M. Barrett, N. J. Bunin, A. Chew, V. E. Gonzalez, Z. Zheng, S. F. Lacey, Y. D. Mahnke, J. J. Melenhorst, S. R. Rheingold, A. Shen, D. T. Teachey, B. L. Levine, C. H. June, D. L. Porter, S. A. Grupp, Chimeric antigen receptor T cells for sustained remissions in leukemia. *N. Engl. J. Med.* **371**, 1507–1517 (2014).
2. B. Hou, Y. Tang, W. Li, Q. Zeng, D. Chang, Efficiency of CAR-T therapy for treatment of solid tumor in clinical trials: A meta-analysis. *Dis. Markers* **2019**, 3425291 (2019).
3. P. Berraondo, V. Umansky, I. Melero, Changing the tumor microenvironment: New strategies for immunotherapy. *Cancer Res.* **72**, 5159–5164 (2012).
4. D. I. Gabrilovich, S. Nagaraj, Myeloid-derived suppressor cells as regulators of the immune system. *Nat. Rev. Immunol.* **9**, 162–174 (2009).
5. C. M. Diaz-Montero, M. L. Salem, M. I. Nishimura, E. Garrett-Mayer, D. J. Cole, A. J. Montero, Increased circulating myeloid-derived suppressor cells correlate with clinical cancer stage, metastatic tumor burden, and doxorubicin-cyclophosphamide chemotherapy. *Cancer Immunol. Immunother.* **58**, 49–59 (2009).
6. R. Colen, I. Foster, R. Gatenby, M. E. Giger, R. Gillies, D. Gutman, M. Heller, R. Jain, A. Madabhushi, S. Madhavan, S. Napel, A. Rao, J. Saltz, J. Tatum, R. Verhaak, G. Whitman, NCI Workshop Report: Clinical and computational requirements for correlating imaging phenotypes with genomics signatures. *Transl. Oncol.* **7**, 556–569 (2014).
7. Y. Yuan, Spatial heterogeneity in the tumor microenvironment. *Cold Spring Harb. Perspect. Med.* **6**, a026583 (2016).
8. M. Nishino, S. Cardarella, S. E. Dahlberg, D. M. Jackman, N. H. Ramaiya, H. Hatabu, M. S. Rabin, P. A. Jnne, B. E. Johnson, Radiographic assessment and therapeutic decisions at RECIST progression in EGFR-mutant NSCLC treated with EGFR tyrosine kinase inhibitors. *Lung Cancer* **79**, 283–288 (2013).
9. A. M. Saucedo, J. De La Cerda, H. Suami, R. E. Serda, Multimodal imaging of the tumor microenvironment and biological responses to immune therapy. *Biomed. Microdevices* **20**, 105 (2018).
10. P. Lambin, R. T. H. Leijenaar, T. M. Deist, J. Peerlings, E. E. C. de Jong, J. van Timmeren, S. Sanduleanu, R. T. H. M. Larue, A. J. G. Even, A. Jochems, Y. van Wijk, H. Woodruff, J. van Soest, T. Lustberg, E. Roelofs, W. van Elmpt, A. Dekker, F. M. Mottaghy, J. E. Wildberger, S. Walsh, Radiomics: The bridge between medical imaging and personalized medicine. *Nat. Rev. Clin. Oncol.* **14**, 749–762 (2017).
11. J. J. M. van Griethuysen, A. Fedorov, C. Parmar, A. Hosny, N. Aucoin, V. Narayan, R. G. H. Beets-Tan, J. C. Fillion-Robin, S. Pieper, H. J. W. L. Aerts, Computational radiomics system to decode the radiographic phenotype. *Cancer Res.* **77**, e104–e107 (2017).
12. R. Parihar, C. Rivas, M. Huynh, B. Omer, N. Lapteva, L. S. Metelitsa, S. M. Gottschalk, C. M. Rooney, NK cells expressing a chimeric activating receptor eliminate mdscs and rescue impaired CAR-T cell activity against solid tumors. *Cancer Immunol. Res.* **7**, 363–375 (2019).
13. K. B. Ghaghada, Z. A. Starosolski, A. Lakoma, C. Kaffes, S. Agarwal, K. K. Athreya, J. Shohet, E. Kim, A. Annapragada, Heterogeneous uptake of nanoparticles in mouse models of pediatric high-risk neuroblastoma. *PLOS ONE* **11**, e0165877 (2016).
14. E. J. Moding, D. P. Clark, Y. Qi, Y. Li, Y. Ma, K. Ghaghada, G. A. Johnson, D. G. Kirsch, C. T. Badea, Dual-energy micro-computed tomography imaging of radiation-induced vascular changes in primary mouse sarcomas. *Int. J. Radiation Oncol.* **85**, 1353–1359 (2013).
15. I. Scarfo, M. V. Maus, Current approaches to increase CAR T cell potency in solid tumors: Targeting the tumor microenvironment. *J. Immunother. Cancer* **5**, 28 (2017).
16. T. L. Whiteside, The tumor microenvironment and its role in promoting tumor growth. *Oncogene* **27**, 5904–5912 (2008).
17. V. Pistoia, F. Morandi, G. Bianchi, A. Pezzolo, I. Prigione, L. Raffaghello, Immunosuppressive microenvironment in neuroblastoma. *Front. Oncol.* **3**, 167 (2013).
18. A. Heczey, C. U. Louis, B. Savoldo, O. Dakhova, A. Durett, B. Grilley, H. Liu, M. F. Wu, Z. Mei, A. Gee, B. Mehta, H. Zhang, N. Mahmood, H. Tashiro, H. E. Heslop, G. Dotti, C. M. Rooney, M. K. Brenner, CAR T cells administered in combination with lymphodepletion and PD-1 inhibition to patients with neuroblastoma. *Mol. Ther. J. Amer. Soc. Gene Ther.* **25**, 2214–2224 (2017).
19. F. C. Thistlethwaite, D. E. Gilham, R. D. Guest, D. G. Rothwell, M. Pillai, D. J. Burt, A. J. Byatte, N. Kirillova, J. W. Valle, S. K. Sharma, K. A. Chester, N. B. Westwood, S. E. R. Halford, S. Nabarro, S. Wan, E. Austin, R. E. Hawkins, The clinical efficacy of first-generation carcinoembryonic antigen (CEACAM5)-specific CAR T cells is limited by poor persistence and transient pre-conditioning-dependent respiratory toxicity. *Cancer Immunol. Immunother.* **66**, 1425–1436 (2017).
20. J. D. Wolchok, A. Hoos, S. O'Day, J. S. Weber, O. Hamid, C. Lebbe, M. Maio, M. Binder, O. Bohnsack, G. Nichol, R. Humphrey, F. S. Hodi, Guidelines for the evaluation of immune therapy activity in solid tumors: Immune-related response criteria. *Clin. Cancer Res.* **15**, 7412–7420 (2009).
21. C. A. Ramos, G. Dotti, Chimeric antigen receptor (CAR)-engineered lymphocytes for cancer therapy. *Expert Opin. Biol. Ther.* **11**, 855–873 (2011).
22. K. B. Ghaghada, C. T. Badea, L. Karumbaiah, N. Fettig, R. V. Bellamkonda, G. A. Johnson, A. Annapragada, Evaluation of tumor microenvironment in an animal model using a nanoparticle contrast agent in computed tomography imaging. *Acad. Radiol.* **18**, 20–30 (2011).
23. C. T. Badea, K. K. Athreya, G. Espinosa, D. Clark, A. P. Ghafoori, Y. Li, D. G. Kirsch, G. A. Johnson, A. Annapragada, K. B. Ghaghada, Computed tomography imaging of primary lung cancer in mice using a liposomal-iodinated contrast agent. *PLOS ONE* **7**, e34496 (2012).
24. D. P. Clark, K. Ghaghada, E. J. Moding, D. G. Kirsch, C. T. Badea, In vivo characterization of tumor vasculature using iodine and gold nanoparticles and dual energy micro-CT. *Phys. Med. Biol.* **58**, 1683–1704 (2013).
25. F. Orlhac, F. Frouin, C. Nioche, N. Ayache, I. Buvat, Validation of a method to compensate multicenter effects affecting CT radiomics. *Radiology* **291**, 53–59 (2019).
26. R. Sun, E. J. Limkin, M. Vakalopoulou, L. Dercle, S. Champiat, S. R. Han, L. Verlingue, D. Brandao, A. Lancia, S. Ammari, A. Hollebecque, J. Y. Scoazec, A. Marabelle, C. Massard, J. C. Soria, C. Robert, N. Paragios, E. Deutsch, C. Ferté, A radiomics approach to assess tumour-infiltrating CD8 cells and response to anti-PD-1 or anti-PD-L1 immunotherapy: An imaging biomarker, retrospective multicohort study. *Lancet Oncol.* **19**, 1180–1191 (2018).
27. S. Trebeschi, S. G. Drago, N. J. Birkbak, I. Kurilova, A. M. Călin, A. Delli Pizzi, F. Lalezari, D. M. J. Lambregts, M. W. Rohaan, C. Parmar, E. A. Rozeman, K. J. Hartemink, C. Swanton, J. B. A. G. Haanen, C. U. Blank, E. F. Smit, R. G. H. Beets-Tan, H. J. W. L. Aerts, Predicting response to cancer immunotherapy using non-invasive radiomic biomarkers. *Annals. Encol.* **30**, 998–1004 (2019).
28. M. Ravanelli, D. Farina, M. Morassi, E. Roca, G. Cavalleri, G. Tassi, R. Maroldi, Texture analysis of advanced non-small cell lung cancer (NSCLC) on contrast-enhanced computed tomography: prediction of the response to the first-line chemotherapy. *Eur. Radiol.* **23**, 3450–3455 (2013).
29. F. Giganti, P. Marra, A. Ambrosi, A. Salerno, S. Antunes, D. Chiari, E. Orsenigo, A. Esposito, E. Mazza, L. Albarello, R. Nicoletti, C. Staudacher, A. del Maschio, F. de Cobelli, Pre-treatment MDCT-based texture analysis for therapy response prediction in gastric cancer: Comparison with tumour regression grade at final histology. *Eur. J. Radiol.* **90**, 129–137 (2017).
30. M. L. Tremblay, C. Davis, C. V. Bowen, O. Stanley, C. Parsons, G. Weir, M. Karkada, M. M. Stanford, K. D. Brewer, Using MRI cell tracking to monitor immune cell recruitment in response to a peptide-based cancer vaccine. *Magn. Reson. Med.* **80**, 304–316 (2018).
31. A. Heczey, D. Liu, G. Tian, A. N. Courtney, J. Wei, E. Marinova, X. Gao, L. Guo, E. Yvon, J. Hicks, H. Liu, G. Dotti, L. S. Metelitsa, Invariant NKT cells with chimeric antigen receptor provide a novel platform for safe and effective cancer immunotherapy. *Blood* **124**, 2824–2833 (2014).
32. T. Zhang, A. Barber, C. L. Sentman, Generation of antitumor responses by genetic modification of primary human T cells with a chimeric NKG2D receptor. *Cancer Res.* **66**, 5927–5933 (2006).
33. D. R. Shaffer, B. Savoldo, Z. Yi, K. K. H. Chow, S. Kakarla, D. M. Spencer, G. Dotti, M. F. Wu, H. Liu, S. Kenney, S. Gottschalk, T cells redirected against CD70 for the immunotherapy of CD70-positive malignancies. *Blood* **117**, 4304–4314 (2011).
34. P. F. Kelly, J. Carrington, A. Nathwani, E. F. Vanin, RD114-pseudotyped oncoretroviral vectors. Biological and physical properties. *Ann N Y Acad Sci* **938**, 262–276 (2001).
35. N. Lapteva, A. G. Durett, J. Sun, L. A. Rollins, L. L. Huye, J. Fang, V. Dandekar, Z. Mei, K. Jackson, J. Vera, J. Ando, M. C. Ngo, E. Coustan-Smith, D. Campana, S. Szmania, T. Garg,

A. Moreno-Bost, F. Vanrhee, A. P. Gee, C. M. Rooney, Large-scale ex vivo expansion and characterization of natural killer cells for clinical applications. *Cytotherapy* **14**, 1131–1143 (2012).

36. Y. Xu, M. Zhang, C. A. Ramos, A. Durett, E. Liu, O. Dakhova, H. Liu, C. J. Creighton, A. P. Gee, H. E. Heslop, C. M. Rooney, B. Savoldo, G. Dotti, Closely related T-memory stem cells correlate with in vivo expansion of CAR.CD19-T cells and are preserved by IL-7 and IL-15. *Blood* **123**, 3750–3759 (2014).
37. M. G. Lechner, D. J. Liebertz, A. L. Epstein, Characterization of cytokine-induced myeloid-derived suppressor cells from normal human peripheral blood mononuclear cells. *J. Immunol.* **185**, 2273–2284 (2010).
38. V. Bronte, S. Brandau, S. H. Chen, M. P. Colombo, A. B. Frey, T. F. Greten, S. Mandruzzato, P. J. Murray, A. Ochoa, S. Ostrand-Rosenberg, P. C. Rodriguez, A. Sica, V. Umansky, R. H. Vonderheide, D. I. Gabrilovich, Recommendations for myeloid-derived suppressor cell nomenclature and characterization standards. *Nat. Commun.* **7**, 12150 (2016).
39. J. S. Miller, C. M. Rooney, J. Curtsinger, R. McElmurry, V. McCullar, M. R. Verneris, N. Lapteva, D. McKenna, J. E. Wagner, B. R. Blazar, J. Tolar, Expansion and homing of adoptively transferred human natural killer cells in immunodeficient mice varies with product preparation and in vivo cytokine administration: implications for clinical therapy. *Biol. Blood Marrow Transplant.* **20**, 1252–1257 (2014).
40. C. T. Badea, D. P. Clark, M. Holbrook, M. Srivastava, Y. Mowery, K. B. Ghaghada, Functional imaging of tumor vasculature using iodine and gadolinium-based nanoparticle contrast agents: a comparison of spectral micro-CT using energy integrating and photon counting detectors. *Phys. Med. Biol.* **64**, 065007 (2019).

Acknowledgments: We would like to acknowledge P. Sarkar and Texas Children's Hospital Small Animal Imaging Facility for help with micro-CT imaging and Baylor College of Medicine Pathology Core for help with IHC. **Funding:** Texas Children's Hospital Pediatric Pilot Research Award, American Cancer Society (MRSG-16-196-01-LIB), and the NIH (NCI/NIDCR 1U01DE028233-01). **Author contributions:** Guarantor of integrity of entire study: K.B.G. and R.P.; study concepts/study design or data acquisition or data analysis/interpretation: all authors; manuscript drafting or manuscript revision for important intellectual content: all authors; approval of final version of submitted manuscript: all authors; literature research: K.B.G., Z.S., and R.P.; experimental studies: L.D., Z.S., C.H.R., I.S., K.B.G., and R.P.; statistical analysis: Z.S., K.B.G., and R.P.; manuscript editing: all authors. **Competing interests:** The authors declare that they have no competing interests. **Data and materials availability:** All data needed to evaluate the conclusions in the paper are present in the paper and/or the Supplementary Materials. Additional data related to this paper may be requested from the authors.

Submitted 18 December 2019
Accepted 27 May 2020
Published 10 July 2020
10.1126/sciadv.aba6156

Citation: L. Devkota, Z. Starosolski, C. H. Rivas, I. Stupin, A. Annapragada, K. B. Ghaghada, R. Parihar, Detection of response to tumor microenvironment–targeted cellular immunotherapy using nano-radiomics. *Sci. Adv.* **6**, eaba6156 (2020).